Electron-phonon coupling in $Mn_{1-x}Fe_xSi$

Nazir Khan,[1,*] O. De la Peña-Seaman,[2] Rolf Heid,[1] David Voneshen,[3,4] Ayman H. Said,[5] Andreas Bauer,[6,7] Tobias Konrad,[6] Michael Merz,[1,8] Thomas Wolf,[1] C. Pfleiderer,[6,7,9,10] and Frank Weber[1,†]

[1]*Institute for Quantum Materials and Technologies, Karlsruhe Institute of Technology, D-76131 Karlsruhe, Germany*
[2]*Instituto de Fisica, Benemerita Universidad Autonoma de Puebla, Apartado Postal J-48, 72570 Puebla, Puebla, Mexico*
[3]*ISIS Facility, Rutherford Appleton Laboratory, Chilton, Didcot, Oxfordshire OX11 0QX, United Kingdom*
[4]*Department of Physics, Royal Holloway University of London, Egham TW20 0EX, United Kingdom*
[5]*Advanced Photon Source, Argonne National Laboratory, Lemont, Illinois 60439, USA*
[6]*Physik Department, Technische Universität München, D-85748 Garching, Germany*
[7]*Centre for Quantum Engineering (ZQE), Technische Universität München, D-85748 Garching, Germany*
[8]*Karlsruhe Nano Micro Facility (KNMFi), Karlsruhe Institute of Technology, D-76131 Karlsruhe, Germany*
[9]*MCQST, Technische Universität München, D-85748 Garching, Germany*
[10]*Heinz Maier-Leibnitz Zentrum (MLZ), Technische Universität München, D-85748 Garching, Germany*

We present a study of the lattice dynamical properties of $Mn_{1-x}Fe_xSi$ with $0 \leqslant x \leqslant 0.22$. Employing time-of-flight neutron spectroscopy and inelastic x-ray scattering, we investigate the doping dependence of phonon energies, E_{ph}, and linewidths, Γ_{ph}. We find anomalous softening and broadening of a phonon mode propagating along the [111] direction. *Ab initio* lattice dynamical calculations link this softening to an enhanced electron-phonon coupling due to the doping-dependent changes of the Fermi surface. We discuss an interplay of increased electron-phonon coupling and reduced ordered magnetic moments in $Mn_{1-x}Fe_xSi$.

I. INTRODUCTION

The family of transition-metal monosilicides (TM-Si) $Mn_{1-x}Fe_xSi$ crystallizing in the cubic B20 structure (#198) hosts rich physics associated with the spin and charge degrees of freedom. The realization of magnetic skyrmions as the first example of topologically protected spin textures in the cubic chiral magnet MnSi [1] has opened a new avenue for spintronic applications [2]. On the other hand, suppression of helical magnetic order in MnSi via pressure has led to the discovery of novel states of matter such as partial magnetic order [3] and a non-Fermi liquid without quantum criticality [4]. The same magnetic order is continuously suppressed by substitutional doping of MnSi with Fe yielding a magnetic quantum critical point at the critical concentration $x_c^{Fe} \approx 0.17$ [5–7]. Recent *ab initio* calculations predict that TM-Si compounds (TM = Fe, Co, Mn, Re, Ru) host topological bulk and surface phonons [8].

While magnetic properties of $Mn_{1-x}Fe_xSi$ at $x \leqslant 0.22$ have been studied in detail by elastic and inelastic neutron scattering (INS), knowledge about the lattice dynamical properties is limited. Raman scattering was used to study the end members of the series, MnSi [9] and FeSi [10]. The latter has been investigated more closely by INS because of its unusual non-magnetic ground state. Indeed, phonon renormalization upon heating has been observed [11] in FeSi powder samples. In studies of single-crystalline FeSi, the sensitivity of a particular phonon mode propagating along the [111] direction to the temperature-induced magnetic fluctuations was reported [12] followed by a recent more comprehensive analysis of INS data [13]. This magnetically induced phonon renormalization in FeSi motivated us to investigate the lattice dynamics in helimagnetic $Mn_{1-x}Fe_xSi$. The high sensitivity of the magnetic phenomena to extrinsic parameters such as chemical pressure/doping and the absence of sudden structural changes make this compound series ideal for scrutinizing lattice dynamical properties.

II. EXPERIMENTAL AND CALCULATIONAL DETAILS

The lattice constants of $Mn_{1-x}Fe_xSi$ were determined on samples prepared from polycrystalline rods [14] by means of Rietveld refinements of data collected on a Huber G670 diffractometer in Guinier geometry with Mo $K\alpha$ radiation. To investigate lattice dynamics in single-crystalline $Mn_{1-x}Fe_xSi$, we employed neutron time-of-flight (TOF) and high-resolution inelastic x-ray scattering (IXS) for various doping levels $0 \leqslant x \leqslant 0.22$. The single-crystalline samples were grown using the Bridgeman method [7,15] ($x = 0, 0.09$) and the optical floating-zone technique [16,17] ($x = 0.16, 0.19, 0.22$). Neutron TOF scattering experiments were performed on the MERLIN spectrometer located at the ISIS neutron facility, Rutherford Appleton Laboratory [18]. Experimental raw data are available for download [19]. Samples were aligned with the [110]-[001] plane being horizontal. Measurements were done in HORACE mode [20] rotating the sample over 70° around the vertical axis. IXS experiments were carried out at the HERIX spectrometer, beamline 30-ID located at the Advanced Photon Source, Argonne National

*nazirkhan91@gmail.com
†frank.weber@kit.edu

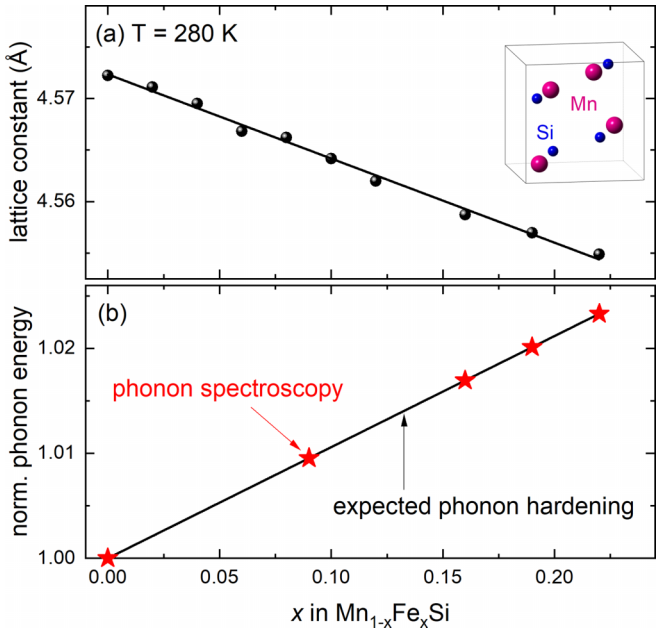

FIG. 1. (a) Lattice constant of $Mn_{1-x}Fe_xSi$ determined by XRD performed at $T = 280$ K. The line is a linear fit to the data. The inset displays the cubic unit cell of $Mn_{1-x}Fe_xSi$ (space group No. 198). (b) Expected hardening of phonons (normalized at $x = 0$) because of the decreasing value of the lattice constant with doping (see text, calculated with a Grüneisen parameter $\gamma_G = 2$). Red asterisks denote the doping values that were investigated by inelastic neutron and/or x-ray spectroscopy.

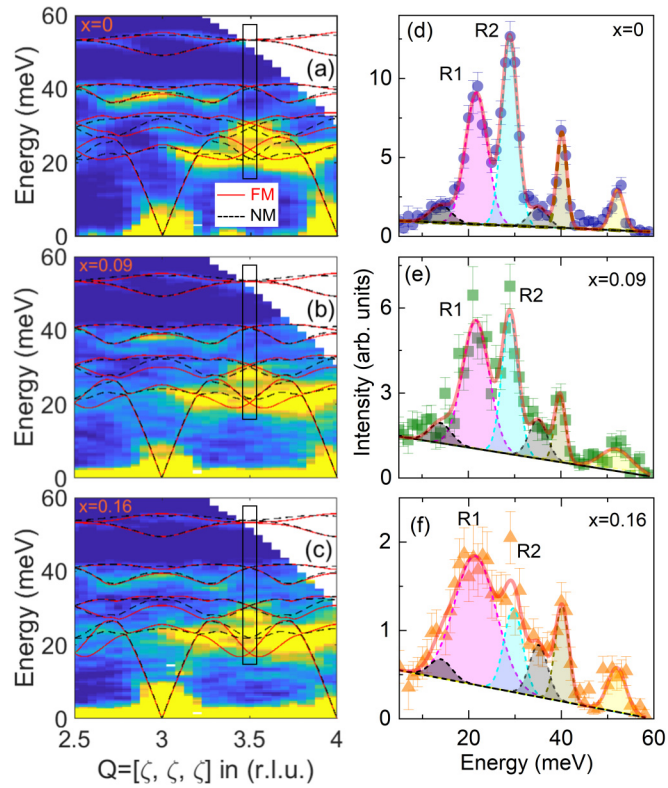

FIG. 2. (a), (b), and (c) exhibit observed neutron-scattering intensities (color-coded: bright yellow, high; dark blue, low) along $\mathbf{Q} = [\zeta, \zeta, \zeta]$, $2.5 \leqslant \zeta \leqslant 4.0$ at $T = 300$ K in $Mn_{1-x}Fe_xSi$, with (a) $x = 0$, (b) 0.09, and (c) 0.16. Solid and dashed lines denote calculated dispersions with and without spin polarization, respectively. Calculations shown in (b) and (c) were done for $x = 0.10$ and 0.15, respectively. (d)–(f) Intensities at the R point averaged for wave vectors $\mathbf{Q} = (H, H, H)$ and $H = 2.5$ and 3.5 [marked by rectangular boxes in (a)–(c)] for $x = 0$, 0.09, and 0.16, respectively. The fits (solid lines) consist of Gaussian peaks (dashed lines) on top of a linear background (thick solid lines). Labels $R1$ and $R2$ mark the peaks subsequently investigated by IXS. Gray peaks were identified as the background signal in MnSi (see text) and approximated with fixed values for the energy and width for $x = 0.09$ and 0.16.

Laboratory. IXS energy scans were performed at constant wave vector $\boldsymbol{Q} = \boldsymbol{\tau} + \boldsymbol{q}$, where $\boldsymbol{\tau}$ is a reciprocal lattice point and $\boldsymbol{q}$ is the phonon wave vector in the first Brillouin zone (BZ). Phonon excitations were approximated by damped harmonic oscillator (DHO) functions convoluted with the experimental resolution function. The electronic and lattice dynamical properties were calculated via density-functional perturbation theory (DFPT) as implemented in the mixed basis pseudopotential (MBPP) code. Calculations were done including collinear spin polarization predicting the ordered magnetic moment. It is known that such calculations overestimate the ordered moment. Therefore, we also calculated the electronic properties via the full-potential linearized augmented plane-wave (LAPW) method implemented in the ELK code. Here, we applied a spin-scaling factor (ssxc) in the exchange-correlation potential to fix the ordered magnetic moment to the experimental one. More details on the experimental and theoretical techniques are discussed in Appendixes A, B, and C.

III. RESULTS—EXPERIMENT

The phonon energies represent the binding strength between the atoms. Therefore, we typically expect that phonon energies increase, i.e., harden when the lattice constants shrink, for instance when the crystal temperature is lowered [13]. For $Mn_{1-x}Fe_xSi$, the lattice constants decrease by about 0.4% near room temperature in the doping range $0 \leqslant x \leqslant 0.22$ [Fig. 1(a)]. Though chemical substitution can have more profound effects than only changing the lattice constants, the simple expectation of phonon hardening for decreasing lattice constants is often found true when the masses of the substituted elements are similar and electronic effects are small [21–23]. Thus, in the absence of electron-phonon-coupling effects, we would expect a typical hardening of the phonon energies of 2.2% for $0 \leqslant x \leqslant 0.22$ using a Grüneisen parameter of 2 [Fig. 1(b)]. Indeed, we show in Appendix C that such an increase is predicted for the average phonon energy $\bar{\omega} = \int \omega F(\omega) d\omega$ in our nonmagnetic calculations featuring negligible coupling between electrons and phonons [$F(\omega)$: phonon density of states].

Figures 2(a)–2(c) show neutron-scattering intensities along the [111] direction. INS (as well as IXS; see below) data in $Mn_{1-x}Fe_xSi$ generally show complex intensity distributions because lattice excitations with finite structure factors are close in energy and often cannot be analyzed separately. Only a few high-symmetry points such as the zone boundary along the [111] direction, i.e., the R point at $\mathbf{q} = (0.5, 0.5, 0.5)$,

offer clear phonon spectra with well-separated peaks. There are four longitudinal phonon modes distributed over nearly 40 meV at the R point [Fig. 2(d)]. The R point will be the focus of our analysis where we observe anomalous phonon softening and broadening in one of the modes at this point in reciprocal space (see below).

We analyze neutron TOF data combined from R points at $\mathbf{Q} = (2.5, 2.5, 2.5)$ and (3.5,3.5,3.5) for $x = 0$ [Fig. 2(d)], $x = 0.09$ [Fig. 2(e)], and $x = 0.16$ [Fig. 2(f)]. Both spectra feature the same four phonon peaks and can be added together for better statistics. In MnSi, the peaks are well separated and can be analyzed in detail [Fig. 2(d)]. The data for $Mn_{0.91}Fe_{0.09}Si$ and $Mn_{0.84}Fe_{0.16}Si$ show larger statistical error bars that result from the strongly reduced sample mass of $m \approx 20$ and 6 g, respectively, compared to $m \approx 52$ g for the MnSi single crystal used also in a previous investigation [15]. Nevertheless, we find that the two lowest modes, which we call $R1$ ($E_{R_1} < 25$ meV) and $R2$ ($E_{R_1} \approx 30$ meV) for simplicity, overlap more strongly in our data for $x = 0.16$ than for $x = 0$. The $R1$ mode seems to soften and broaden as a function of doping [Figs. 2(d)–2(f)]. However, the low statistics for the doped samples as well as some additional backscattering around 14 and 35 meV [gray peaks in Figs. 2(d)–2(f); see Appendix A and Table I for more details] make a precise analysis difficult.

Therefore, we performed IXS experiments on single crystals of $Mn_{1-x}Fe_xSi$ with $x = 0$, 0.09, 0.16, 0.19, and 0.22 as IXS offers both better energy resolution ($\Delta E_{\mathrm{IXS}} = 1.4$ meV) and better momentum resolution ($\Delta q_{\mathrm{IXS}} = 0.09$ Å^{-1}) than the MERLIN spectrometer ($\Delta E_{\mathrm{INS}} \approx 3.8$ meV at $E = 20$ meV; $\Delta q_{\mathrm{INS}} = 0.27$ Å^{-1} for data shown in this report) for our investigation. IXS spectra taken at the R point, $\mathbf{Q} = (2.5, 2.5, 2.5)$ [Fig. 3(a)], and close to Γ, $\mathbf{Q} = (2, 2, 0.05)$ [Fig. 3(b)] show well-defined lattice excitations and permit a straightforward analysis [symbols in Figs. 3(c) and 3(d)]. Phonon spectra collected at other high-symmetry points, i.e., M at $\mathbf{q} = (0.5, 0.5, 0)$ and X at $\mathbf{q} = (0.5, 0, 0)$, can be found in Appendix B (Figs. 5 and 6). In comparison to the expected hardening [straight solid line in Fig. 3(c)], we find a diverse behavior of the Γ- and R-point phonons [symbols in Fig. 3(c)]. The $\Gamma1$ and $R2$ modes have an essentially doping-independent energy whereas the $\Gamma2$ mode hardens by about 4%. The $R1$ mode softens by about 5% and, thus, IXS corroborates what the neutron TOF data indicated.

The resolution function in IXS experiments is practically independent of the energy transfer (see Appendix B) and therefore is well suited for the investigation of zone boundary phonons with flat dispersions. Thus, we can deduce the linewidth of the DHO function representing the intrinsic properties of a phonon [symbols in Fig. 3(d)]. The linewidth of the modes close to the zone center stays unchanged under increasing x, whereas the linewidths increase for the modes around the R point. The increase of the $R1$ mode's linewidth is more than twice as large as that measured for the $R2$ mode.

The linewidth Γ of a phonon is proportional to the inverse of its lifetime τ. In the harmonic limit, τ is infinite and the phonon excitations observed in an energy scan via INS or IXS are resolution limited. In real materials, the phonon lifetime is affected by lattice anharmonicity but also disorder can reduce τ and increase Γ. In metals, the coupling between electrons and phonons, well known for mediating conventional superconductivity, can also reduce the excitations' lifetime. Here, we argue that electron-phonon coupling (EPC) is the most likely cause of the observed softening and broadening of the $R1$ mode. Changes in the lattice constants typically affect all phonons the same way and yield harder phonon energies for increasing doping values in $Mn_{1-x}Fe_xSi$. Thus, the structural evolution with doping cannot explain the softening of the $R1$ mode. Chemical disorder introduced by doping could lead to increasing phonon linewidths. But, again, one expects this to be a general trend and not mode selective. On the other hand, EPC is well known to be highly mode—as well as momentum—selective.

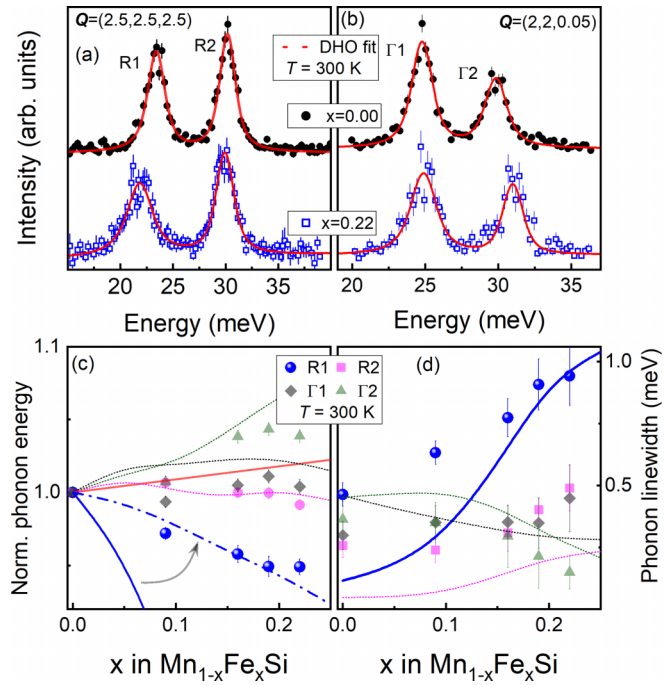

FIG. 3. (a),(b) IXS spectra taken at the R point, $\mathbf{Q} = (2.5, 2.5, 2.5)$, and close to the Γ point, $\mathbf{Q} = (2, 2, 0.05)$, respectively, for $Mn_{1-x}Fe_xSi$, $x = 0$ and 0.22, and $T = 300$ K. The solid lines are fits to the data consisting of DHO functions convoluted with the experimental resolution on top of a linear background. (c) Doping dependence of phonon energies, E_{ph} (normalized at $x = 0$) obtained from our analysis (symbols). Solid and short-dashed lines refer to DFPT calculations for the modes given in the legend. The dash-dotted line corresponds to the solid line with the calculated softening reduced by a factor of 6. The straight line in (c) denotes the expected evolution based on experimental lattice constants and a typical Grüneisen parameter of 2. (d) Phonon linewidth of the approximated DHO functions (symbols) compared to the calculated linewidth due to EPC (lines) for the two R and Γ modes.

IV. RESULTS—THEORY

Our experimental results show that the doping dependence of phonon energies in $Mn_{1-x}Fe_xSi$ is more complex than the simple hardening estimated based on the evolution of the lattice constants [see Fig. 3(c)]. Previous work [24] showed that phonon dispersions in undoped MnSi are well described by *ab initio* calculations based on DFPT. Further, it was reported that spin-polarized calculations predicting a ferromagnetic ground

state show a slightly improved agreement compared to nonmagnetic calculations.

Here, we present equivalent spin-polarized and nonmagnetic calculations that were extended to $Mn_{1-x}Fe_xSi$ for $x = 0.05$, 0.1, 0.15, and 0.2 via the self-consistent virtual crystal approximation [21,25] (see Appendix C for details). The results for the phonon dispersion calculated with (solid lines) and without (dashed lines) spin polarization are overlaid with experimental data in Figs. 2(a)–2(c). Only branches with longitudinal symmetry are shown due to all other modes exhibiting zero structure factors. We find good agreement between experiment and theory similar to previous work [24]. The differences between the nonmagnetic and spin-polarized calculations [dashed and solid lines in Figs. 2(a)–2(c), respectively] are small at most wave vectors with the prominent exception of the $R1$ mode in the spin-polarized calculations. The nonmagnetic calculations predict hardening whereas the spin-polarized theory shows a large softening as a function of doping. As we will show below, the predicted softening of the $R1$ mode is due to an enhanced EPC as evidenced by an increase of the phonon linewidth. In the nonmagnetic calculations, EPC is small in MnSi and even decreases with Fe doping. Thus, we find, similar to our previous work in FeSi [12], that spin-polarized calculations capture anomalous lattice dynamics in $Mn_{1-x}Fe_xSi$ and discuss only results from such magnetic calculations in the following.

Ab initio lattice dynamical calculations take the phonon eigenvectors into account and offer additional insights on the evolution of the phonon properties under doping, going beyond the general hardening estimated from the evolution of the lattice constants. Furthermore, we can compute $\gamma_{\mathrm{EPC}}^{\boldsymbol{q},\lambda}$, the electronic contribution to the linewidth of a phonon in the dispersion branch λ and wave vector $\boldsymbol{q}$, as

$$\gamma_{\mathrm{EPC}}^{\boldsymbol{q},\lambda} = \pi\omega_{q\lambda}\sum_{\vec{k}}\left|g^{q\lambda}_{\vec{k}+\vec{q},\vec{k}}\right|^2\delta(\epsilon_{\vec{k}}-\epsilon_F)\delta(\epsilon_{\vec{k}+\vec{q}}-\epsilon_F) \quad (1)$$

with the EPC matrix element $g^{\vec{q}\lambda}_{\vec{k}+\vec{q},\vec{k}}$ and the electronic joint density of states (eJDOS), defined by $\sum_{\vec{k}}\delta(\epsilon_{\vec{k}}-\epsilon_F)\,\delta(\epsilon_{\vec{k}+\vec{q}}-\epsilon_F)$.

Corresponding calculations for the doping-dependent phonon energies and linewidths are overplotted with the results deduced from IXS in Figs. 3(c) and 3(d). Theory correctly predicts the trends of harder, nearly constant, and softer phonon energies with doping for the $\Gamma 2$, the $\Gamma 1$ and $R2$ modes, and the $R1$ mode, respectively. However, the softening of the $R1$ mode is overestimated by a factor of 6 [see the solid blue and dash-dotted blue lines in Fig. 3(c)]. Regarding the calculated linewidths, we find that the trends as a function of doping are correct for the $R1$, $R2$, and $\Gamma 2$ modes. For $\Gamma 1$ it is opposite but we note that both predictions and observations for all modes except $R1$ feature only small changes of the linewidth of 0.25 meV or less over the whole doping range investigated. For the $R1$ mode we predict a larger broadening of nearly 1 meV over the investigated doping range in comparison to an experimentally observed broadening of 0.5 meV [blue symbols and solid line in Fig. 3(d)].

Summarizing, our calculations generally are in good qualitative agreement with our experimental findings and further corroborate that doping-dependent EPC softens and broadens

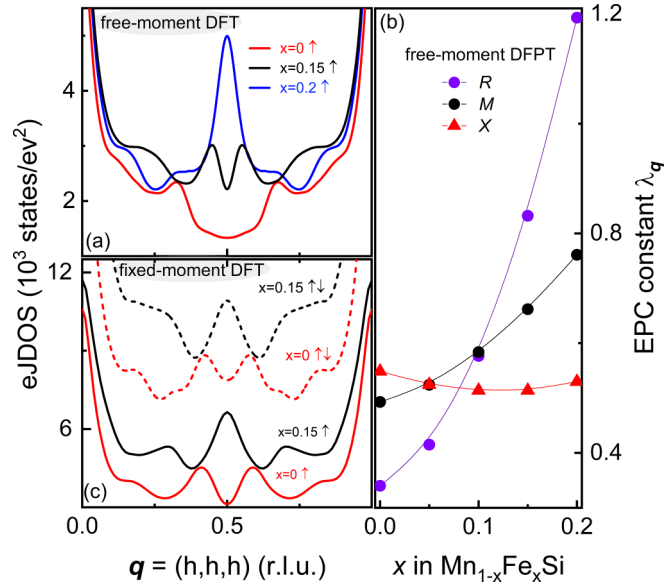

FIG. 4. (a) Electronic joint density of states (eJDOS) along Γ-R-Γ calculated via free-moment DFT for $x = 0$, 0.15, and 0.2 in $Mn_{1-x}Fe_xSi$. Up arrow indicates that only one spin channel (majority spin) contributes. (b) Doping dependence of the momentum-resolved EPC constant λ_q at the R, M, and X high-symmetry points predicted by the free-moment DFPT calculations. Solid lines are guides to the eye. (c) eJDOS predicted by fixed-moment DFT calculations for $x = 0$ and 0.15. Dashed lines represent results with contributions from spin-up and spin-down states at the Fermi surface. Solid lines show the results only for electronic states of the majority spin-up direction.

the $R1$ mode. However, the predicted phonon renormalization is stronger than observed.

The lattice dynamical calculations offer a deeper look into the origin of the phonon renormalization in $Mn_{1-x}Fe_xSi$. $\gamma_{\mathrm{EPC}}^{\boldsymbol{q},\lambda}$ is governed by the intrinsic coupling strength of the phonon mode given by $g^{\vec{q}\lambda}_{\vec{k}+\vec{q},\vec{k}}$ and the eJDOS, which is often also referred to as the Fermi surface (FS) nesting function [26] and related to the imaginary part of the electronic susceptibility [27]. We show the calculated eJDOS along Γ-R-Γ in Fig. 4(a). We note that our *ab initio* calculations predict a fully polarized electronic band structure. Thus, the eJDOS originates only from the majority spin-up channel. The calculations predict a clear increase of the eJDOS at the R point, $\mathbf{q} = (0.5, 0.5, 0.5)$, with doping and a strong FS nesting for $x = 0.2$ ($\mathrm{eJDOS}_{R,x=0.2}/\mathrm{eJDOS}_{R,\,x=0} \approx 3.8$). The momentum-resolved EPC constant $\lambda_{\mathbf{q}}$ at wave vectors corresponding to the R, M, and X points reveals a strong increase at R with x ($\lambda_{R,x=0.2}/\lambda_{R,x=0} \approx 3.5$), a moderate increase at M, and nearly constant value at X [Fig. 4(b)]. Thus, we conclude that the phonon broadening at R is, within DFPT calculations, driven by the eJDOS and the calculated band structure of $Mn_{0.8}Fe_{0.2}Si$ features a strong FS nesting.

However, it is a known shortcoming of standard density-functional theory (DFT) calculations to overestimate the ordered magnetic moment by a factor of about 2.5. For instance, our calculations predict an ordered moment of $1.0\,\mu_B$ per Mn whereas a value of $0.41\mu_B$ is observed [6,17] (see

Table II and Appendix C). Recently, the FS of MnSi was investigated by de Haas–van Alphen measurements [28]. Corresponding calculations with the ordered magnetic moment fixed to the experimental value of $0.41\mu_B$ per Mn ion reproduced the experimentally deduced FS very well. Thus, we compared our calculated Fermi surface for MnSi [Fig. 9(a)] with the reported one [28] and found clear discrepancies. We were able to reproduce the reported Fermi surface employing the full-potential LAPW method implemented in the ELK code [Figs. 8(c) and 8(e)]. Here, we use a spin-scaling factor (ssxc) in the exchange-correlation potential to fix the ordered moment to the observed value (for details, see Appendix C and Fig. 7). In the spin-scaled-moment calculations, both spin channels contribute to the eJDOS shown in Fig. 4(c) along the Γ-R-Γ direction. Here, the eJDOS at the R point increases with doping only by a factor of about 2.1 in the spin-up channel [solid lines in Fig. 4(c)]. Thus, the increase of the eJDOS with Fe doping indicates an increase of EPC also in spin-scaled-moment calculations. The reduced strength of the FS nesting feature is in line with the smaller phonon renormalization observed experimentally. Unfortunately, a full lattice dynamical calculation including EPC based on this altered electronic band structure is not yet implemented in the code and, thus, beyond the scope of this work. But we expect that calculations based on the spin-scaled-moment band structure will show a reduced softening of the $R1$ mode compared to that predicted in the standard free-moment DF(P)T.

To conclude, our lattice dynamical calculations point towards a FS nesting developing with doping as the origin of the increasing EPC in $Mn_{1-x}Fe_xSi$. Although the effect is overestimated, calculations with a spin-scaled ordered magnetic moment predict a more modest but still significant increase of the eJDOS at the R point.

V. DISCUSSION

The $R1$ phonon featuring the anomalous softening and broadening as a function of Fe doping [see Fig. 3(c)] is the same for which an anomalous softening and broadening as a function of temperature was observed in FeSi [13,29]. In contrast to FeSi, the anomalous behavior for $Mn_{1-x}Fe_xSi$ does not extend to the $R2$ nor to the $\Gamma1$ modes, which is in agreement with our lattice dynamical calculations. Comparing our results to those of FeSi, one has to keep in mind that the extended phonon softening in FeSi in the temperature range $T = 100 - 300$ K is due to metallization, i.e., an increased screening of the interatomic forces at the crossover from a low-temperature insulating to a high-temperature metallic phase [11,13,30]. For $Mn_{1-x}Fe_xSi$, the resistivity at room temperature increases with doping [31] and, thus, an increased screening cannot explain the observed softening.

A similarity to FeSi is that lattice dynamical calculations only capture qualitatively the observed anomalies if performed with spin polarization, i.e., for a magnetically ordered system. Experimentally, FeSi does not show magnetic order at any temperature and $Mn_{1-x}Fe_xSi$ only at temperatures a factor of 10 or more below room temperature where we performed our measurements. Magnetic fluctuations present in both FeSi and $Mn_{1-x}Fe_xSi$ seem to be relevant for the lattice dynamical properties. While calculations assuming a full magnetic order may overestimate the impact of magnetism, completely nonmagnetic calculations miss the anomalous behavior altogether. Unfortunately, lattice dynamical calculations in a disordered paramagnet are not possible in our code. We discussed a magnetic origin of phonon renormalization previously [12], i.e., the question whether the presence of a magnetic exchange interaction J might affect, i.e., harden, the phonon energies. Suppressing J by doping might then lead to the reverse effect, i.e., phonon softening. This question is worth pursuing since the origin of the phonon softening would be magnetic but cannot be answered within our current report. However, it will be very difficult to distinguish magnetically induced softening and that due to EPC since a change of the ordered magnetic moment will modify the electronic band structure and, thus, electron-phonon coupling.

Our results highlight EPC and the evolution of the Fermi surface as the origin of the renormalization of the $R1$ phonon mode with doping. While the strong tendency towards Fermi surface nesting predicted by MBPP calculations [see Fig. 4(a)] is unreliable concerning the largely overestimated ordered magnetic moment (see Table II), the effect of a moderately increasing eJDOS at the R point is a robust feature also present in our LAPW-based calculations [see Fig. 4(c)]. Similar calculations using a spin-scaling factor successfully described the doping dependence of the anomalous and topological Hall signal for $x \leqslant 0.4$ [32], quantities which are highly sensitive to the FS topology. Implementing full lattice dynamical calculations based on the LAPW method with spin scaling is a project beyond the scope of the current report. However, first estimates for the $R1$ mode via the frozen-phonon method based on the LAPW-calculated electronic structure indicate that the renormalization of the phonon energy with doping is only half of that predicted by MBPP calculations and, thus, significantly closer to experimental observations.

In itinerant ferromagnets magnetic order and EPC are both mediated by conduction electrons. Kim and co-workers published a couple of reports investigating this scenario theoretically in the 1980 s [33–36]. Most prominently, they found in model calculations that EPC reduces the magnetization, potentially by up to $1\mu_B$ per magnetic ion. Thus, what is the impact of an increased EPC to the reduced and finally suppressed ordered magnetic moment in $Mn_{1-x}Fe_xSi$? Our MBPP calculations predict a reduction of the ordered magnetic moment by $0.2\,\mu_B$ per Mn ion for $x = 0.2$ (Table II) accompanied by an increase of the overall, i.e., energy- and momentum-integrated EPC from $\lambda_{EPC} = 0.69$ for $x = 0$ to $\lambda_{EPC} = 0.84$ for $x = 0.2$. Yet, the increase of EPC is, at least for the R point, clearly overestimated. Therefore, we need to wait for full lattice dynamical calculations based on the spin-scaled electronic structure to establish a correlation between the EPC and the ordered magnetic moment in $Mn_{1-x}Fe_xSi$.

VI. CONCLUSION

In summary, the present study establishes that $Mn_{1-x}Fe_xSi$ exhibits intriguing lattice dynamical properties, showcasing EPC induced by Fe doping. In sharp contrast to the doping-dependent decrease of the lattice constants of $Mn_{1-x}Fe_xSi$, a significant softening and broadening of a phonon mode propagating along the [111] direction is observed. Based on

TABLE I. Approximated parameters for the phonon modes observed by inelastic neutron scattering. Fit functions are shown in Fig. 2 and described in more detail in Appendix A.

	$x = 0$		$x = 0.09$		$x = 0.16$	
Mode/peak	Energy (meV)	Linewidth (meV)	Energy (meV)	Linewidth (meV)	Energy (meV)	Linewidth (meV)
$R1$	21.7 ± 0.1	5.6 ± 0.4	21.6 ± 0.2	6.7 ± 0.7	21.4 ± 0.7	10.6 ± 3.7
$R2$	28.9 ± 0.1	3.9 ± 0.2	29.0 ± 0.2	4.1 ± 0.4	29.6 ± 0.5	4.7 ± 1.4
$R3$	40.2 ± 0.1	2.5 ± 0.2	39.8 ± 0.2	2.8 ± 0.6	40.2 ± 0.2	3.5 ± 0.4
$R4$	52.2 ± 0.2	3.4 ± 0.5	51.9 ± 1.2	7.9 ± 3.0	51.9 ± 0.3	4.6 ± 0.5

our electronic structure and lattice dynamical calculations, we ascribe the phonon renormalization in $Mn_{1-x}Fe_xSi$ to increasingly strong EPC linked to changes of the Fermi surface geometry upon doping. Spin-polarized calculations can reproduce this trend, which is completely absent in nonmagnetic calculations. However, a more quantitative assessment of EPC needs to wait until lattice dynamical calculations that take into account the spin-scaling method are available. In such calculations, the impact of EPC on the ordered magnetic moment will be an interesting question to be addressed.

ACKNOWLEDGMENTS

We wish to thank M. A. Wilde for helpful discussions. This work has been funded by the Deutsche Forschungsgemeinschaft (DFG, German Research Foundation) under Project No. 419331252 and under TRR80 (From Electronic Correlations to Functionality, Project No. 107745057), TRR360 (Constrained Quantum Matter, Project No. 492547816), SPP2137 (Skyrmionics, Project No. 403191981, Grant No. PF393/19), DFG-GACR WI3320/3-1 (Project No. 323760292), and the excellence cluster MCQST under Germany's Excellence Strategy EXC-2111 (Project No. 390814868). Financial support by the European Research Council (ERC) through Advanced Grants No. 291079 (TOP-FIT) and No. 788031 (ExQuiSid) is gratefully acknowledged. Experiments at the ISIS Pulsed Neutron and Muon Source were supported by a beamtime allocation from the Science and Technology Facilities Council [19]. This research used resources of the Advanced Photon Source, a U.S. Department of Energy (DOE) Office of Science User Facility operated for the DOE Office of Science by Argonne National Laboratory under Contract No. DE-AC02-06CH11357.

APPENDIX A: INELASTIC NEUTRON SCATTERING

High-quality single crystals of $Mn_{1-x}Fe_xSi$ with $x = 0$, 0.09, and 0.16 weighing about 52, 20, and 6 g were used for the INS experiments. INS measurements were performed on the direct-geometry, TOF chopper spectrometer MERLIN at the Rutherford Appleton Laboratory in Harwell, UK [18]. The MERLIN detectors cover scattering angles from -45° to $+135^\circ$ horizontally and $\pm 30^\circ$ vertically. The samples were mounted on an Al sample holder using thin Al foil and Al sheet with the (110)-(001) plane of the single crystal as the horizontal scattering plane. Measurements were taken at room temperature only. All data [19] were taken with an incident energy $E_i = 71.2$ meV and covering approximately the same volume of reciprocal space by rotating each sample over 70° with angular steps of 0.25°. We used a Gd chopper and a frequency of $f = 400$ Hz was chosen to record data. The raw data were corrected for detector efficiency by normalizing the intensities using a standard vanadium sample. Data was reduced using the MANTID package [37] and analyzed using HORACE [20]. Scattering wave vectors $\boldsymbol{Q} = \boldsymbol{\tau} + \boldsymbol{q}$, where τ is a reciprocal lattice vector and $\mathbf{q}$ is the reduced wave vector in the first BZ, are expressed in reciprocal lattice units $(2\pi/a,\ 2\pi/b,\ 2\pi/c)$ with the lattice constants $a = b = c = 4.55$ Å of the cubic unit cell (undoped MnSi).

Data for $\mathbf{Q} = (H, H, H)$ show four well-defined peaks for MnSi in agreement with the calculated structure factors. However, some additional scattering is present at around 14 and 35 meV. Such scattering can appear due to scattering involving the sample and the sample holder (made out of aluminum) and, thus, is not eliminated by subtracting an empty-can scan [38]. Whereas the corresponding intensities are small compared to the phonon scattering for pure MnSi, the lower scattering rates in doped samples require that we account for this scattering in a consistent way. Therefore, we approximated the additional scattering around 14 and 35 meV by two additional peaks, obtained the peak parameters for pure MnSi [gray-shaded peaks in Fig. 2(d)], and fixed the energy and width in our analysis of the data for $x = 0.09$ and 0.16 [gray-shaded peaks in Figs. 2(e) and 2(f)]. The approximated parameters for the energies and linewidths of the four phonon modes are presented in Table I.

APPENDIX B: INELASTIC X-RAY SCATTERING

The IXS experiments were carried out at the 30-ID beamline, HERIX spectrometer [39], at the Advanced Photon Source, Argonne National Laboratory, with a focused beam size of 15 μm × 35 μm. The incident energy was 23.74 keV [40] and the horizontally scattered beam was analyzed by a spherically curved silicon analyzer (Reflection 12 12 12) [41]. The full width at half maximum (FWHM) of the energy and wave-vector space resolution was about 1.4 meV and 0.09 $Å^{-1}$, respectively, where the former is experimentally determined by scanning the elastic line of a piece of Plexiglas and the latter is calculated from the experiment geometry and incident energy. Phonon excitations measured in constant-momentum scans were approximated by DHO functions [42] convoluted with a pseudo-Voigt resolution function

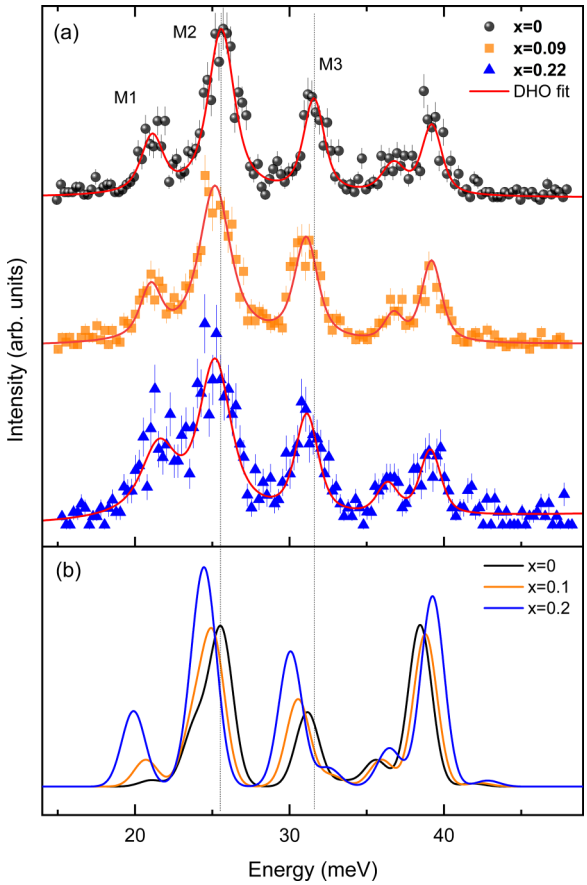

FIG. 5. (a) IXS spectra (solid symbols) at the M point, $\mathbf{Q} = (2.5, 2.5, 0)$, measured for $x = 0$, 0.09, and 0.22. Solid lines are fits to the data consisting of the DHO function convoluted with the experimental resolution on top of a linear background. (b) Spin-polarized calculations of the M point phonon structure factors at $\mathbf{Q} = (2.5, 2.5, 0)$ for $x = 0$, 0.1, and 0.2. Finite structure factors are visualized by resolution-limited Gaussian peaks. Both experiment and theory indicate phonon softening for the $M2$ and $M3$ modes.

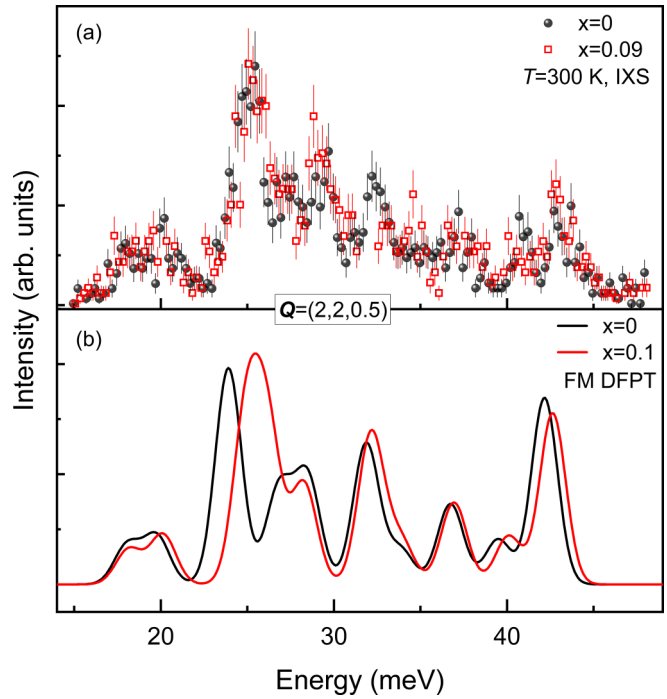

FIG. 6. (a),(b) IXS spectra (solid symbols) at the X point, $\mathbf{Q} = (2, 2, 0.5)$, measured for $x = 0$ and 0.09. (b) Spin-polarized calculations of the X point phonon structure factors at $\mathbf{Q} = (2, 2, 0.5)$ for $x = 0$ and 0.1. The experiment reveals the phonon modes with energies close to that predicted by the spin-polarized DFPT calculations for $x = 0$ and 0.1.

(FWHM = 1.4 meV). The resolution function was further used to approximate resolution-limited elastic scattering at zero energy transfer. Measurements were done at scattering wave vectors $\boldsymbol{Q} = \boldsymbol{\tau} + \boldsymbol{q}$, where τ is a reciprocal lattice vector and $\mathbf{q}$ is the reduced wave vector in the first BZ. Wave vectors are expressed in reciprocal lattice units $(2\pi/a,\ 2\pi/b,\ 2\pi/c)$ with the lattice constants $a = b = c = 4.55$ Å of the cubic unit cell (undoped MnSi). We used high-quality single-crystal samples. For $x = 0$, 0.09, and 0.16, the IXS samples were prepared from the specimen previously used for our INS measurements. Samples with $x = 0.19$ and 0.22 were grown the same way as that for 0.16, i.e., by the floating-zone method at the Technical University of Munich. All IXS specimen were thinned down to a thickness of about 100 μm to allow x-ray scattering in transmission. The samples were mounted in air.

Measured energy spectra at constant-momentum transfer were approximated using a pseudo-Voigt function for the resolution-limited elastic peak and a DHO function [42] for the phonon peaks. The DHO function was convoluted with the fit of the experimental resolution function. The DHO function is

$$S(Q, \omega) = \frac{[n(\omega) + 1]Z(Q)4\omega\Gamma/\pi}{\left[\omega^2 - \tilde{\omega}_q^2\right]^2 + 4\omega^2\Gamma^2}, \qquad \text{(B1)}$$

where $\boldsymbol{Q}$ and ω are the wave vector and energy transfer, respectively, $n(\omega)$ is the Bose function, Γ is the imaginary part of the phonon self-energy, $\tilde{\omega}_q$ is the phonon energy renormalized by the real part of the phonon self-energy, and $Z(\boldsymbol{Q})$ is the phonon structure factor. This function covers the energy loss and energy gain scattering by a single line shape. The intensity ratio of the phonon peaks at $E = \pm\omega_q$ is fixed by the principle of detailed balance. The energy ω_q of the damped phonons is obtained from the fit parameters of the DHO function by $\omega_q = \sqrt{\tilde{\omega}_q^2 - \Gamma^2}$ [43].

Data were collected at high-symmetry points R, M, X, i.e., at $\boldsymbol{q} = (0.5, 0.5, 0.5)$, $(0.5, 0.5, 0)$, $(0, 0, 0.5)$ and close to the Γ point at $\boldsymbol{\tau} = (2, 2, 0)$. Only the scans shown in the main text, i.e., at the R [$\boldsymbol{Q} = (2.5, 2.5, 2.5)$] and close to the Γ point [$\boldsymbol{Q} = (2, 2, 0.05)$], yielded data where phonon energies and linewidths could be determined unambiguously. Figures 5 and 6 show exemplary data taken at the M and X points, respectively, along with the respective calculated phonon intensity distributions. The calculations for $x = 0$ at M [black line in Fig. 5(b)] and $x = 0.1$ at X [black line in Fig. 6(b)] emphasize that phonons around 25 meV, which might be interesting as comparison to the behavior of the $R1$ mode, cannot be analyzed in detail because peaks are overlapping. Nevertheless, the calculations predict that the dominating peak near 25 meV at the M point softens in doped samples [Fig. 5(b)]. On the

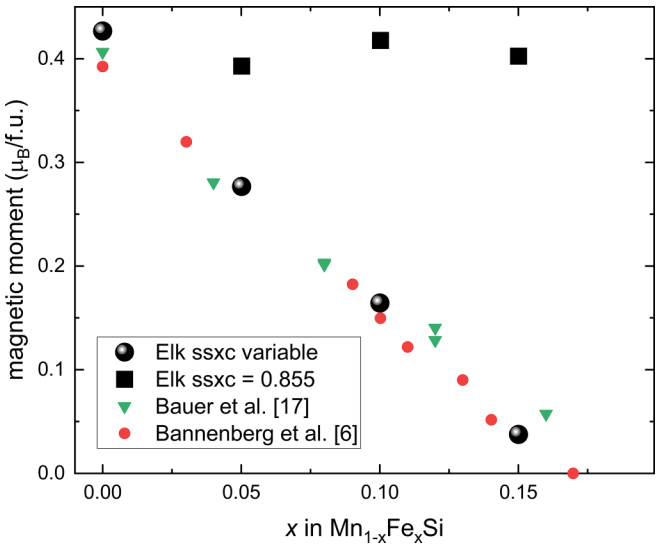

FIG. 7. Ordered magnetic moment of $Mn_{1-x}Fe_xSi$ from experiment (triangles [17], dots [6]) and calculated values applying a fixed (squares) and a variable ssxc factor (spheres).

other hand, the 25-meV peak at the X point shifts to higher energies for $x = 0.09$ [Fig. 6(b)]. Both predictions are in qualitative agreement with the experimental data [Figs. 5(a) and 6(a)]. Thus, our lattice dynamical calculations do predict the trends of the doping dependence in $Mn_{1-x}Fe_xSi$ correctly.

APPENDIX C: COMPUTATIONAL DETAILS, AVERAGE PHONON ENERGY, ORDERED MAGNETIC MOMENTS, AND CALCULATED FERMI SURFACES

The present calculations are based on DFT [44,45] and were performed by two different methods. First, the lattice dynamics and electron-phonon coupling properties were calculated via DFPT [46] as implemented in MBPP code [47–49] including collinear spin polarization. Norm-conserving pseudopotentials for Mn/Fe and Si were constructed following the scheme of Vanderbilt [50] including Mn/Fe 3s and 3p semicore states in the valence space. Local functions of s, p, and d symmetry at the Mn/Fe sites were supplemented by plane waves up to a kinetic energy of 24 Ry. We note that LDA+U was tested in previous investigations [51,52]. However, a significant reduction of the ordered magnetic moment could only be achieved for unreasonably high values of $U >$ 6–7 eV.

Secondly, the electronic properties were obtained via the full-potential LAPW method implemented within the ELK code [53,54], and applying a spin-scaling factor (ssxc) in the exchange-correlation potential [55–57] to obtain a calculated value of the magnetic moment closer to the experimental one. For MnSi ($m_{expt} \approx 0.4\,\mu B/f.u.$) [6,17], by using ssxc = 0.855 we could reduce the magnetic moment from its generalized gradient approximation (GGA) value of $m_{GGA} = 1\mu_B$/f.u. to $m_{ssxc} \approx m_{expt}$. Similarly, for intermediate Fe content on the alloy ($x = 0.05,0.10,0.15$) the ssxc value was individually adjusted to reproduce the experimental magnetic moment (see

TABLE II. First line: ordered magnetic moment of $Mn_{1-x}Fe_xSi$ as predicted in our *ab initio* calculations for $x = 0 - 0.2$. Second line: ordered magnetic moment of $Mn_{1-x}Fe_xSi$ for $x = 0 - 0.15$ as reported by experiment [6,17] and used for our fixed-moment calculations. The experimentally observed ordered magnetic moment for $x = 0.2$ is zero since the Curie temperature T_C reaches zero temperature at $x_C \approx 0.17$ [5,7].

Methods	$x = 0$	$x = 0.05$	$x = 0.1$	$x = 0.15$	$x = 0.2$
DFT–free moment	1.0	0.95	0.90	0.85	0.8
DFT–fixed moment	0.41	0.28	0.17	0.06	0

Fig. 7 and Table II). Because this approach significantly reduces the ordered magnetic moment, it generates changes on the band structure, i.e., a shift in energy for both spin channels. For the LAPW-ELK calculations, the core states were treated fully relativistically, and the semicore and valence states were computed in a scalar relativistic approximation, neglecting spin-orbit coupling. We chose muffin-tin radii (R_{mt}) of 2.165 and 1.985 a.u. for the transition metal (Mn/Fe) and Si, respectively, and a plane-wave cutoff $R_{mt} \times K_{max} = 7.5$, with K_{max} as the maximum length for the **k** vectors. The angular momentum cutoff for the LAPW functions were expanded up to $l = 12$.

For both methods, the exchange-correlation potential was evaluated within the GGA using the Perdew-Burke-Ernzerhof functional [58], neglecting spin-orbit coupling. The Brillouin-zone integration was performed using a Monkhorst-Pack special **k**-point set of $16 \times 16 \times 16$ with a Gaussian smearing of 0.03 and 0.1 eV for the ELK and MBPP calculations, respectively [59]. Using MBPP, complete phonon dispersions were obtained via standard Fourier interpolation of dynamical matrices calculated on a $4 \times 4 \times 4$ **q**-point

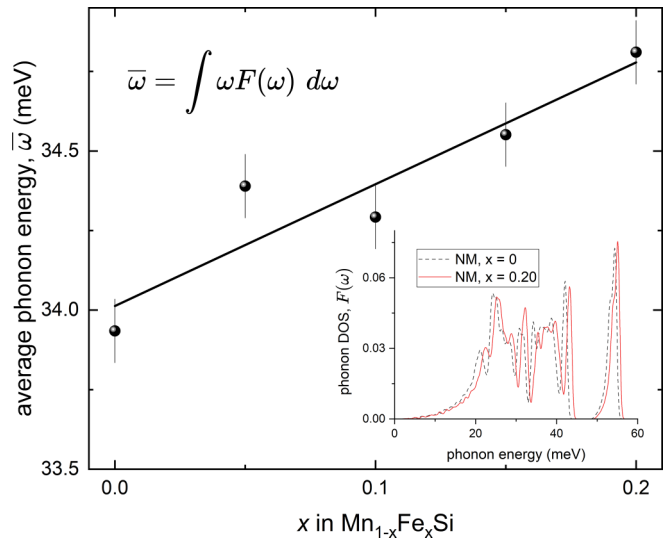

FIG. 8. Average phonon energy $\bar{\omega} = \int \omega F(\omega) d\omega$ from nonmagnetic calculations. The inset shows examples of the computed phonon density of states $F(\omega)$ for two doping levels.

mesh. For the calculations of electron-phonon coupling matrix elements, a denser **k**-point mesh of $32 \times 32 \times 32$ was employed.

The $Mn_{1-x}Fe_xSi$ alloy was modeled in the self-consistent virtual crystal approximation (VCA) [21,25]. In the case of the all-electron method, the Mn ($Z = 25$) sites were substituted by virtual atoms that have a fractional electronic charge ($Z = 25 + x$) depending on the Fe content (x). In order to keep the neutrality of the virtual atom, the valence charge was modified by the same amount. Then, the VCA potential is determined self-consistently for each x without shape approximation [53]. In the same spirit, the VCA was implemented within the pseudopotential method by generating new pseudopotentials with a fractional charge ($Z = 25 + x$) for each x and by adjusting the valence charge accordingly. All results of this study were obtained with experimental lattice constants [60] while the internal parameters were determined via a force-minimization approach for each Fe content (x).

The nonmagnetic calculations feature negligible coupling between phonons and electrons and, thus, can serve as a reference for the expected evolution of the phonon energies in the absence of electronic effects. We calculated the nonmagnetic phonon density of states and deduced the average phonon energy defined by $\bar{\omega} = \int \omega F(\omega) d\omega$ where $F(\omega)$ represents the phonon density of states. We find that $\bar{\omega}(x)$ increases (Fig. 8) similar to our expectations based on the evolution of the lattice constants (Fig. 1).

Calculated Fermi surfaces for $x = 0$ and 0.15 are shown in Fig. 9 based on DFT as implemented in MBPP code [Figs. 9(a) and 9(b)] and the LAPW method implemented in the ELK code using a spin-scaling factor to fix the ordered magnetic moment to that observed in experiment [Figs. 9(c)–9(f)]. In the former, the Fermi surface is fully polarized and only electrons with spin-up are contributing. Calculations applying a spin-scaling factor feature a Fermi surface with both spin-up and spin-down bands. The thus calculated Fermi surface for $x = 0$ [Figs. 9(c) and 9(e)] is in good agreement with calculations and corresponding measurements published recently [28].

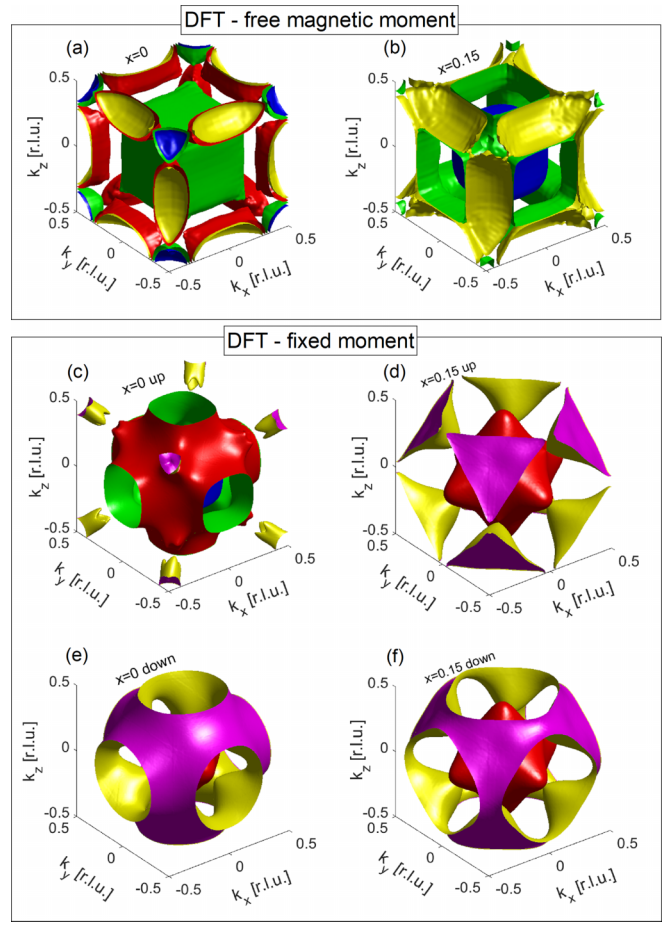

FIG. 9. (a),(b) Fermi surfaces of $Mn_{1-x}Fe_xSi$ predicted by spin-polarized free-moment DFT calculations for $x = 0$ and 0.15, respectively, where the electronic states from the majority spin-up channel only contribute to the Fermi surface. Colors denote different bands crossing the Fermi energy. (c),(d) FS predicted by the fixed-moment DFT calculations for $x = 0$ and 0.15, respectively, where the electronic states belong to the majority spin-up direction. (e),(f) Same as (c),(d) but for the minority spin-down direction.

[1] S. Mühlbauer, B. Binz, F. Jonietz, C. Pfleiderer, A. Rosch, A. Neubauer, R. Georgii, and P. Böni, Skyrmion lattice in a chiral magnet, Science **323**, 915 (2009).

[2] T. Schulz, R. Ritz, A. Bauer, M. Halder, M. Wagner, C. Franz, C. Pfleiderer, K. Everschor, M. Garst, and A. Rosch, Emergent electrodynamics of skyrmions in a chiral magnet, Nat. Phys. **8**, 301 (2012).

[3] L. Pintschovius, D. Reznik, C. Pfleiderer, and H. von Lohneysen, Partial magnetic order in the itinerant-electron magnet MnSi, Pramana **63**, 117 (2004).

[4] C. Pfleiderer, P. Böni, T. Keller, U. K. Rössler, and A. Rosch, Non-Fermi liquid metal without quantum criticality, Science **316**, 1871 (2007).

[5] J. Kindervater *et al.*, Evolution of magnetocrystalline anisotropies in $Mn_{1-x}Fe_xSi$ and $Mn_{1-x}Co_xSi$ as inferred from small-angle neutron scattering and bulk properties, Phys. Rev. B **101**, 104406 (2020).

[6] L. J. Bannenberg, F. Weber, A. J. E. Lefering, T. Wolf, and C. Pappas, Magnetization and ac susceptibility study of the cubic chiral magnet $Mn_{1-x}Fe_xSi$, Phys. Rev. B **98**, 184430 (2018).

[7] L. J. Bannenberg, R. M. Dalgliesh, T. Wolf, F. Weber, and C. Pappas, Evolution of helimagnetic correlations in $Mn_{1-x}Fe_xSi$ with doping: A small-angle neutron scattering study, Phys. Rev. B **98**, 184431 (2018).

[8] T. Zhang, Z. Song, A. Alexandradinata, H. Weng, C. Fang, L. Lu, and Z. Fang, Double-Weyl phonons in transition-metal monosilicides, Phys. Rev. Lett. **120**, 016401 (2018).

[9] H. M. Eiter, P. Jaschke, R. Hackl, A. Bauer, M. Gangl, and C. Pfleiderer, Raman study of the temperature and magnetic-field

dependence of the electronic and lattice properties of MnSi, Phys. Rev. B **90**, 024411 (2014).
[10] D. Menzel, P. Popovich, N. N. Kovaleva, J. Schoenes, K. Doll, and A. V. Boris, Electron-phonon interaction and spectral weight transfer in $Fe_{1-x}Co_xSi$, Phys. Rev. B **79**, 165111 (2009).
[11] O. Delaire, K. Marty, M. B. Stone, P. R. C. Kent, M. S. Lucas, D. L. Abernathy, D. Mandrus, and B. C. Sales, Phonon softening and metallization of a narrow-gap semiconductor by thermal disorder, Proc. Natl. Acad. Sci. USA **108**, 4725 (2011).
[12] S. Krannich *et al.*, Magnetic moments induce strong phonon renormalization in FeSi, Nat. Commun. **6**, 8961 (2015).
[13] N. Khan, S. Krannich, D. Boll, R. Heid, D. Lamago, A. Ivanov, D. Voneshen, and F. Weber, Combined inelastic neutron scattering and *ab initio* lattice dynamics study of FeSi, Phys. Rev. B **105**, 134304 (2022).
[14] A. Bauer, A. Neubauer, W. Münzer, A. Regnat, G. Benka, M. Meven, B. Pedersen, and C. Pfleiderer, Ultra-high vacuum compatible induction-heated rod casting furnace, Rev. Sci. Instrum. **87**, 063909 (2016).
[15] X. Chen, I. Krivenko, M. B. Stone, A. I. Kolesnikov, T. Wolf, D. Reznik, K. S. Bedell, F. Lechermann, and S. D. Wilson, Unconventional Hund metal in a weak itinerant ferromagnet, Nat. Commun. **11**, 3076 (2020).
[16] A. Bauer, G. Benka, A. Regnat, C. Franz, and C. Pfleiderer, Ultra-high vacuum compatible preparation chain for intermetallic compounds, Rev. Sci. Instrum. **87**, 113902 (2016).
[17] A. Bauer, A. Neubauer, C. Franz, W. Münzer, M. Garst, and C. Pfleiderer, Quantum phase transitions in single-crystal $Mn_{1-x}Fe_xSi$ and $Mn_{1-x}Co_xSi$: Crystal growth, magnetization, ac susceptibility, and specific heat, Phys. Rev. B **82**, 064404 (2010).
[18] R. Bewley, T. Guidi, and S. Bennington, MERLIN: A high count rate chopper spectrometer at ISIS, Not. Neutroni Luce Sincrotrone **14**, 22 (2009).
[19] F. Weber, N. Khan, H. Walker, and D. Voneshen, Spin-phonon coupling in $Mn_{1-x}Fe_xSi$ (STFC ISIS Neutron and Muon Source, 2020), https://doi.org/10.5286/ISIS.E.RB2010794.
[20] R. A. Ewings, A. Buts, M. D. Le, J. van Duijn, I. Bustinduy, and T. G. Perring, HORACE: Software for the analysis of data from single crystal spectroscopy experiments at time-of-flight neutron instruments, Nucl. Instrum. Methods Phys. Res. Sect. A **834**, 132 (2016).
[21] O. De La Peña-Seaman, R. De Coss, R. Heid, and K.-P. Bohnen, *Ab initio* study of the structural, electronic, and phononic properties of $Nb_{1-x}Mo_x$ using the self-consistent virtual-crystal approximation, Phys. Rev. B **76**, 174205 (2007).
[22] O. De La Peña-Seaman, R. De Coss, R. Heid, and K.-P. Bohnen, First-principles study of phonons and superconductivity of $Nb_{1-x}Mo_x$ within the virtual-crystal approximation, J. Phys.: Condens. Matter **19**, 476216 (2007).
[23] R. de Coss-Martínez, P. González-Castelazo, O. De la Peña-Seaman, R. Heid, and K. P. Bohnen, Effect of doping on lattice dynamics and electron–phonon coupling of the actinides Ac–Th alloy, J. Phys.: Condens. Matter **29**, 355401 (2017).
[24] D. Lamago, E. S. Clementyev, A. S. Ivanov, R. Heid, J. M. Mignot, A. E. Petrova, and P. A. Alekseev, Lattice dynamics in the itinerant helical magnet MnSi, Phys. Rev. B **82**, 144307 (2010).
[25] O. De la Peña-Seaman, R. de Coss, R. Heid, and K. P. Bohnen, Electron-phonon coupling and two-band superconductivity of Al- and C-doped MgB_2, Phys. Rev. B **82**, 224508 (2010).
[26] D. Kasinathan, J. Kuneš, A. Lazicki, H. Rosner, C. S. Yoo, R. T. Scalettar, and W. E. Pickett, Superconductivity and lattice instability in compressed lithium from Fermi surface hot spots, Phys. Rev. Lett. **96**, 047004 (2006).
[27] M. D. Johannes and I. I. Mazin, Fermi surface nesting and the origin of charge density waves in metals, Phys. Rev. B **77**, 165135 (2008).
[28] M. A. Wilde, M. Dodenhöft, A. Niedermayr, A. Bauer, M. M. Hirschmann, K. Alpin, A. P. Schnyder, and C. Pfleiderer, Symmetry-enforced topological nodal planes at the Fermi surface of a chiral magnet, Nature (London) **594**, 374 (2021).
[29] S. Krannich, D. Lamago, D. Manske, E. Bauer, A. Prokofiev, R. Heid, K. P. Bohnen, and F. Weber, Absence of spin-orbit coupling induced effects on the lattice dynamics in $CePt_3Si$, Phys. Rev. B **92**, 125137 (2015).
[30] R. Wolfe, J. H. Wernick, and S. E. Haszko, Thermoelectric properties of FeSi, Phys. Lett. **19**, 449 (1965).
[31] C. Meingast, Q. Zhang, T. Wolf, F. Hardy, K. Grube, W. Knafo, P. Adelmann, P. Schweiss, and H. v. Löhneysen, in *The Search for New Materials for Thermoelectric Devices*, edited by V. Zlatic and A. Hewson (Springer, Hvar, Croatia, 2009).
[32] C. Franz *et al.*, Real-space and reciprocal-space Berry phases in the Hall effect of $Mn_{1-x}Fe_xSi$, Phys. Rev. Lett. **112**, 186601 (2014).
[33] D. J. Kim, New phonon effect on itinerant-electron ferromagnetism, Phys. Rev. Lett. **47**, 1213 (1981).
[34] D. J. Kim, Electron-phonon interaction and itinerant-electron ferromagnetism, Phys. Rev. B **25**, 6919 (1982).
[35] D. J. Kim, The electron-phonon interaction and itinerant electron magnetism, Phys. Rep. **171**, 129 (1988).
[36] D. J. Kim, Phonon in a ferromagnet carries magnetization, J. Magn. Magn. Mater. **125**, L257 (1993).
[37] O. Arnold *et al.*, Mantid—Data analysis and visualization package for neutron scattering and μSR experiments, Nucl. Instrum. Methods Phys. Res., Sect. A **764**, 156 (2014).
[38] L. Pintschovius *et al.*, Spurious peaks arising from multiple scattering events involving the sample environment in inelastic neutron scattering, J. Appl. Crystallogr. **47**, 1472 (2014).
[39] A. H. Said, H. Sinn, T. S. Toellner, E. E. Alp, T. Gog, B. M. Leu, S. Bean, and A. Alatas, High-energy-resolution inelastic x-ray scattering spectrometer at beamline 30-ID of the Advanced Photon Source, J. Synchrotron Radiat. **27**, 827 (2020).
[40] T. S. Toellner, A. Alatas, and A. H. Said, Six-reflection meV-monochromator for synchrotron radiation, J. Synchrotron Radiat. **18**, 605 (2011).
[41] A. H. Said, H. Sinn, and R. Divan, New developments in fabrication of high-energy-resolution analyzers for inelastic x-ray spectroscopy, J. Synchrotron Radiat. **18**, 492 (2011).
[42] B. Fåk and B. Dorner, Phonon line shapes and excitation energies, Phys. B (Amsterdam, Neth.) **234-236**, 1107 (1997).
[43] G. Shirane, S. Shapiro, and J. Tranquada, *Neutron Scattering with a Triple-Axis Spectrometer* (Cambridge University Press, Cambridge, 2002).
[44] P. Hohenberg and W. Kohn, Inhomogeneous electron gas, Phys. Rev. **136**, B864 (1964).

[45] W. Kohn and L. J. Sham, Self-consistent equations including exchange and correlation effects, Phys. Rev. **140**, A1133 (1965).

[46] S. Baroni, P. Giannozzi, and A. Testa, Green's-function approach to linear response in solids, Phys. Rev. Lett. **58**, 1861 (1987).

[47] B. Meyer, C. Elsässer, F. Lechermann, and M. Fähnle, FORTRAN90 Program for Mixed-Basis Pseudopotential Calculations for Crystals, Max-Planck-Institut für Metallforschung, Stuttgart (unpublished).

[48] R. Heid and K.-P. Bohnen, Linear response in a density-functional mixed-basis approach, Phys. Rev. B **60**, R3709(R) (1999).

[49] R. Heid, K. P. Bohnen, and K. M. Ho, *Ab initio* phonon dynamics of rhodium from a generalized supercell approach, Phys. Rev. B **57**, 7407 (1998).

[50] D. Vanderbilt, Optimally smooth norm-conserving pseudopotentials, Phys. Rev. B **32**, 8412 (1985).

[51] R. D. Collyer and D. A. Browne, Correlations and the magnetic moment of MnSi, Phys. B (Amsterdam, Neth.) **403**, 1420 (2008).

[52] P. Dutta and S. K. Pandey, Investigating the electronic structure of MSi (M = Cr, Mn, Fe & Co) and calculating U_{eff} & J by using cDFT, Comput. Condens. Matter **16**, e00325 (2018).

[53] The Elk Code, http://elk.sourceforge.net/.

[54] T. Müller, S. Sharma, E. K. U. Gross, and J. K. Dewhurst, Extending solid-state calculations to ultra-long-range length scales, Phys. Rev. Lett. **125**, 256402 (2020).

[55] S. Sharma, E. K. U. Gross, A. Sanna, and J. K. Dewhurst, Source-free exchange-correlation magnetic fields in density functional theory, J. Chem. Theory Comput. **14**, 1247 (2018).

[56] L. Ortenzi, I. I. Mazin, P. Blaha, and L. Boeri, Accounting for spin fluctuations beyond local spin density approximation in the density functional theory, Phys. Rev. B **86**, 064437 (2012).

[57] I. J. Onuorah, P. Bonfà, and R. De Renzi, Muon contact hyperfine field in metals: A DFT calculation, Phys. Rev. B **97**, 174414 (2018).

[58] J. P. Perdew, K. Burke, and M. Ernzerhof, Generalized gradient approximation made simple, Phys. Rev. Lett. **77**, 3865 (1996).

[59] C. L. Fu and K. M. Ho, First-principles calculation of the equilibrium ground-state properties of transition metals: Applications to Nb and Mo, Phys. Rev. B **28**, 5480 (1983).

[60] J. F. DiTusa *et al.*, Magnetic, thermodynamic, and electrical transport properties of the noncentrosymmetric *B*20 germanides MnGe and CoGe, Phys. Rev. B **90**, 144404 (2014).